UC San Diego

UC San Diego Previously Published Works

Title

Faraday Rotation Due to Surface States in the Topological Insulator (Bi1–x Sb x)2Te3

Permalink

https://escholarship.org/uc/item/4x30v01g

Journal

Nano Letters, 17(2)

ISSN

1530-6984

Authors

Shao, Yinming
Post, Kirk W
Wu, Jhih-Sheng
et al.

Publication Date

2017-02-08

DOI

10.1021/acs.nanolett.6b04313

Peer reviewed

eScholarship.org Powered by the California Digital Library
University of California

NANO LETTERS

Letter

pubs.acs.org/NanoLett

Faraday Rotation Due to Surface States in the Topological Insulator $(Bi_{1-x}Sb_x)_2Te_3$

Yinming Shao,[*,△] Kirk W. Post,[†] Jhih-Sheng Wu,[†] Siyuan Dai,[†] Alex J. Frenzel,[†] Anthony R. Richardella,[‡] Joon Sue Lee,[‡] Nitin Samarth,[‡] Michael M. Fogler,[†] Alexander V. Balatsky,[¶,§] Dmitri E. Kharzeev,[∥,⊥] and D. N. Basov[△,†]

[△]Department of Physics, Columbia University, New York, New York 10027, United States

[†]Physics Department, University of California-San Diego, La Jolla, California 92093, United States

[‡]Department of Physics, The Pennsylvania State University, University Park, Pennsylvania 16802, United States

[¶]Nordita, KTH Royal Institute of Technology and Stockholm University, Roslagstullsbacken 23, SE-106 91 Stockholm, Sweden

[§]Institute for Materials Science, Los Alamos National Laboratory, Los Alamos, New Mexico 87545, United States

[∥]Department of Physics and Astronomy, Stony Brook University, Stony Brook, New York 11794-3800, United States

[⊥]Department of Physics and RIKEN-BNL Research Center, Brookhaven National Laboratory, Upton, New York 11973, United States

S *Supporting Information*

ABSTRACT: Using magneto-infrared spectroscopy, we have explored the charge dynamics of $(Bi,Sb)_2Te_3$ thin films on InP substrates. From the magneto-transmission data we extracted three distinct cyclotron resonance (CR) energies that are all apparent in the broad band Faraday rotation (FR) spectra. This comprehensive FR-CR data set has allowed us to isolate the response of the bulk states from the intrinsic surface states associated with both the top and bottom surfaces of the film. The FR data uncovered that electron- and hole-type Dirac Fermions reside on opposite surfaces of our films, which paves the way for observing many exotic quantum phenomena in topological insulators.

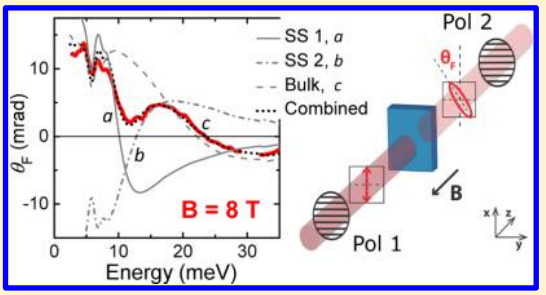

KEYWORDS: *Bismuth antimony telluride, topological insulators, cyclotron resonance, Faraday rotation, topological surface states*

Three-dimensional (3D) topological insulators (TIs) are insulating in the bulk but host gapless, topologically protected surface states (TSSs).[1,2] The Dirac-like TSSs are robust against disorder, as they are protected by topological properties of the bulk electronic wave functions.[3] The linear band dispersion of TSSs[4−6] has been identified by angle resolved photoemission spectroscopy (ARPES), whereas scanning tunneling spectroscopy (STS)[7,8] has verified the distinctive $\sqrt{B}$ dispersing Landau levels (LLs) of the TSS. With the advent of the new generation of thin films of 3D-TIs, it became possible to minimize bulk conduction, yielding an electrodynamic response that is dominated by the TSS.[9−11] However, when surface sensitive probes (ARPES, STS) are applied to these new TI films, they are only able to characterize the top, vacuum-facing surface of the sample. While transport measurements probe all conducting channels in TI thin films, the decomposition of the response to each individual TSS/bulk layer is not trivial.

Here we report on Faraday rotation (FR) and cyclotron resonances (CR) magneto-transmission spectroscopy of $(Bi_{1-x}Sb_x)_2Te_3$ (BST) thin films. The combination of these techniques yields a comprehensive characterization of the TSS dynamics both at the top and bottom surfaces, complementary to transport and ARPES data.[5,6,12−14] We stress that FR, the rotation of light polarization after passing through a medium in magnetic field, is particularly informative in distinguishing multiple conductive channels in complex materials.[15,16] Whereas both CR and FR experiments are sensitive to transitions between the LLs, only the FR allows one to unambiguously discriminate the response of electrons and holes via the sign of the Faraday angle θ_F.[17,18] Additional insights come from the magnetic field dependence of the LL transitions energy (ΔE_n), satisfying the dipole selection rule:[19,20] $\Delta|n| = \pm 1$. For instance, in a system with parabolic bands, including bulk bands in TIs, LL transitions scale linearly with magnetic field as eB/m, where m is the band mass (classical CR). Drastically different LL energies are anticipated and observed for Dirac Fermions in TSSs:[19−21]

$$E_{\pm n} = E_{DP} \pm v_F\sqrt{2e\hbar|n|B} \quad (1)$$

Received: October 14, 2016
Revised: December 28, 2016
Published: December 29, 2016

Downloaded via UNIV OF CALIFORNIA SAN DIEGO on July 21, 2018 at 03:02:12 (UTC).
See https://pubs.acs.org/sharingguidelines for options on how to legitimately share published articles.

© 2016 American Chemical Society

DOI: 10.1021/acs.nanolett.6b04313
Nano Lett. 2017, 17, 980−984

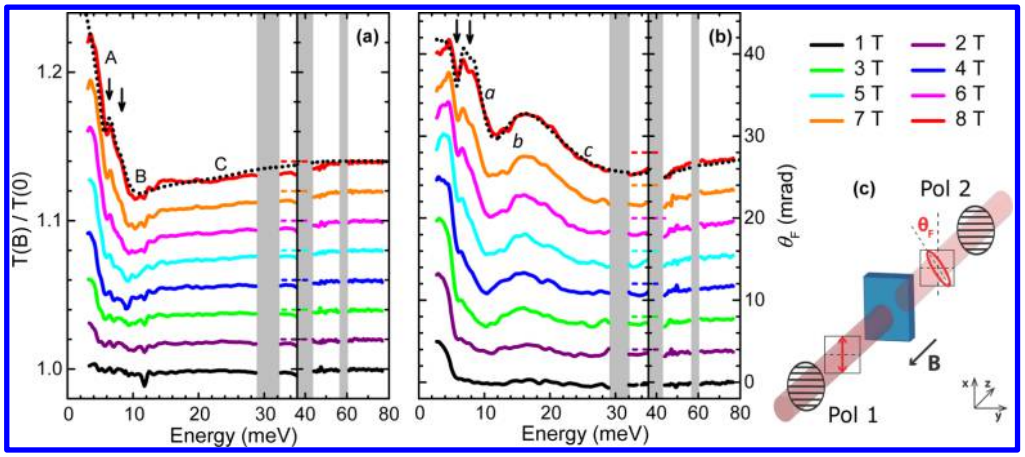

Figure 1. (a) Magneto-transmission data normalized by the spectrum at zero field of the BST thin film. (b) Faraday rotation (FR) data. Data at different fields are offset by (a) 0.02 and (b) 4 mrad for clarity. Opaque regions due to InP absorption are greyed-out. Black dotted lines are Drude–Lorentz model fits for 8 T data and black arrows indicate the positions of infrared active phonons (~6 and 8 meV). (c) Schematic showing the FR definition and measurement setup.

where E_{DP} is the Dirac Point energy, n is the LL index, v_F is the Fermi velocity, and B is the magnetic field. Therefore, TSS/bulk carriers can be further distinguished by their dispersion of LL transition energies with magnetic field ($\sqrt{B}$/linear in B).

Recently, we used terahertz/far-infrared transmission spectroscopy to study the dynamic response of BST thin films grown on InP (111)A substrates (see Supporting Information Sec. I for more details). We found an exceptionally small Drude weight that lies within the upper limit imposed by the conductivity sum rule for TSS.[9] Although the sum rule criterion is instructive, this analysis does not allow one to discriminate between the contributions due to the surface and the bulk. In this work, we disentangle these contributions based on their unique, dynamic responses in a magnetic field. The broadband FR-CR measurements enable a multicomponent analysis of the data and uncover marked distinctions between top and bottom TSSs in our films. The two surfaces have different Fermi energies and host Dirac Fermions of opposite sign, which is required for an observation of a number of exotic effects, including topological exciton condensation in TIs.[6,22]

Generally, multiple types of carriers (electrons/holes in TSS/bulk bands) can coexist in TIs and all contribute to the magneto-optical (MO) response. According to the Drude–Lorentz (DL) model, the total conductivity is the sum of oscillators:

$$\sigma_{xx}(\omega, B) = \sum_{j=1}^{N} \frac{D_j}{\pi} \frac{\gamma_j - i\omega}{\omega_{c,j}^2 - (\omega + i\gamma_j)^2} - \sum_{j=1}^{N} \frac{i\omega\omega_{p,j}^2\varepsilon_0}{\omega_{o,j}^2 - \omega^2 - i\omega\Gamma_j} - i\omega\varepsilon_0(\varepsilon_\infty - 1) \quad (2)$$

$$\sigma_{xy}(\omega, B) = \sum_{j=1}^{N} \frac{D_j}{\pi} \frac{-\omega_{c,j}}{\omega_{cj}^2 - (\omega + i\omega\gamma_j)^2} \quad (3)$$

The first term in eqs 2 and 3 stands for the Drude response of free carriers in magnetic field. Each oscillator is characterized by its own Drude weight ($D_j = \pi ne^2/m$), cyclotron frequency $\omega_{c,j} = qB/m$, and scattering rate γ_j. The second term in eq 2 represents Lorentzian oscillators centered at $\omega_{o,j}$, with plasma frequency $\omega_{p,j}$ and scattering rate Γ_j. The Lorentzian terms describe the contributions of phonons and are absent in the Hall conductivity σ_{xy}. The high frequency dielectric constant ε_∞ accounts for absorptions above the measured frequency range and is associated with interband transitions. In eq 2, each of the Drude oscillators can describe a CR/LL transition in the classical/quantum regime. The model implies that the Drude absorption peak is shifted from zero frequency at $B = 0$ to finite cyclotron frequency ω_c in the presence of an external magnetic field. Similar multicomponent models have been used to successfully decode the complex MO spectrum for multilayer graphene[17] and Bi_2Se_3 thin films.[10]

In the far-infrared region under the thin-film approximation, the measured broadband CR and FR spectra are directly related to real part of $\sigma_{xx}(\omega, B)$ and $\sigma_{xy}(\omega, B)$, respectively. For simplicity, σ_{xx} and σ_{xy} will be assumed to be the real part of the corresponding complex functions in the rest of this Letter.

Magneto-transmission spectra normalized by the spectrum at zero field $T(\omega, B)/T(\omega, 0)$ are shown in Figure 1a. The most prominent field-induced features can be identified in the spectrum obtained at $B = 8$ T: a marked increase (~10%, labeled as A) in the transmission is observed at low frequency, followed by a dip (B) and a weak downturn (C) at higher frequencies. The gross features of the experimental data are accounted for within the Drude model of the cyclotron resonance (eq 2). Both A and B features can be identified in the data at smaller fields. As the magnetic field increases (from 2 to 8 T), the positions of these features increase: an observation consistent with the multicomponent CR interpretation of the observed features. The black arrows in Figure 1 indicate the position of two phonon modes (~6 and 8 meV) in BST.[9] The phonon frequencies do not exhibit frequency shifts with magnetic field.

Faraday rotation spectra, shown in Figure 1b, offer complementary insights into the magneto-optical response. In addition to the low-frequency phonons (arrows), one can readily observe three inflection points (a, b, and c) below 30 meV. Each inflection point corresponds to a peak in σ_{xx} associated with an underlying CR/LL transition.[10,17] All three inflection points harden with increasing magnetic field.

The highest measured FR angle in the low-frequency limit of our data (~15 mrad) is an order of magnitude smaller compared to previous work on Bi_2Se_3.[10] We remark that the quantized FR is expected to occur in multiples of $\alpha \approx 7$ mrad

DOI: 10.1021/acs.nanolett.6b04313
Nano Lett. 2017, 17, 980–984

both in graphene and TIs in the limit of $\omega \ll \omega_c, E_g$,[23,24] where E_g is the energy gap associated with the bulk response. The experimental observation of quantized FR has been reported recently in different TI systems at THz frequencies.[25−27] In this work, the condition $\omega \ll \omega_c$ is not strictly fulfilled since the lowest experimental frequency (~3 meV) is still very close to ω_c (~8 meV) at 8 T due to the broadness of the resonance. Therefore, the observed small rotation is unlikely to be related to quantized FR. Below we will demonstrate that the small rotation is the result of an interplay of multiple transitions, clearly resolved in our broadband spectra, yielding both negative and positive FRs.

We used the DL model (eqs 2 and 3) to fit the CR and FR spectra at each measured magnetic field. The minimum model required to fit both data sets contains three different Drude oscillators. A plausible interpretation of these three oscillators is in terms of three conduction channels associated with the bulk, top, and bottom surfaces of our films. In Figure 2a,b we plot each of these three contributions along with the experimental data at 8 T (red solid line).

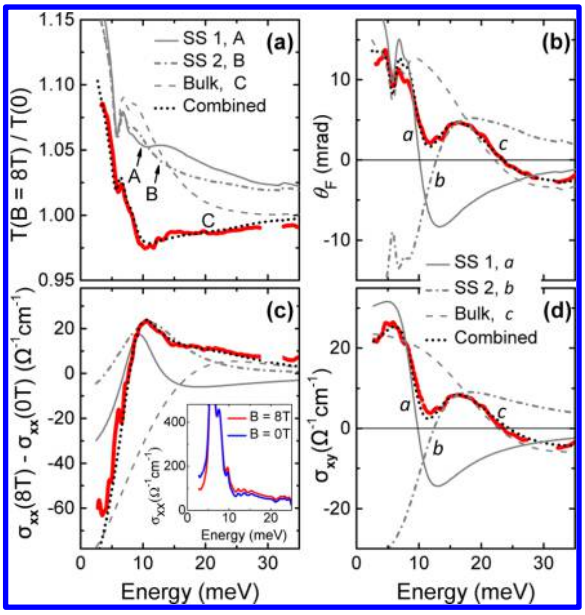

Figure 2. Experimental and modeling results for (a) transmission and (b) FR spectra at 8 T using multicomponent Drude−Lorentz model. In each panel, the red solid line is the data and black dotted line is the fit. Dashed gray lines represent contributions from the bulk. Solid and dash-dotted gray lines represent contributions from the two surfaces states. In panel (c) we plot the difference between the diagonal conductivity (σ_{xx}) spectra obtained at 8 T and at 0 T. The inset displays σ_{xx} at 8 and 0 T, which are dominated by phonons (6 and 8 meV) of BST. In panel (d) the Hall conductivity (σ_{xy}) is plotted. In (b) and (d) the signal from SS 2 (n-type) is opposite in sign compared to SS 1 and bulk (p-type).

The coexistence of three mobile carriers in BST is particularly evident from the decomposition of the fit for θ_F (Figure 2b). The gross features of the spectra are well described by the multicomponent FR response.[17] Specifically, the two features with negative slopes (*a* and *c*) attest to two distinct p-type carriers with different Drude weight and scattering rate. We depict these contributions with the solid and dashed gray lines, respectively. The hump feature with positive slope (*b*) originates from n-type carriers and is indicated with the gray dash-dotted line. In the limit of small Faraday rotation ($\theta_F \ll 1$ rad),[28] the total rotation angle equals the sum of rotations due to the three terms *a*, *b*, and *c*. This net rotation (black dotted line) reproduced all features of our data (red line). The very same parameter set also captures the behavior of magneto-transmission spectra in Figure 2a. All fitting parameters for different magnetic fields are summarized in Figure 3 (see fits for

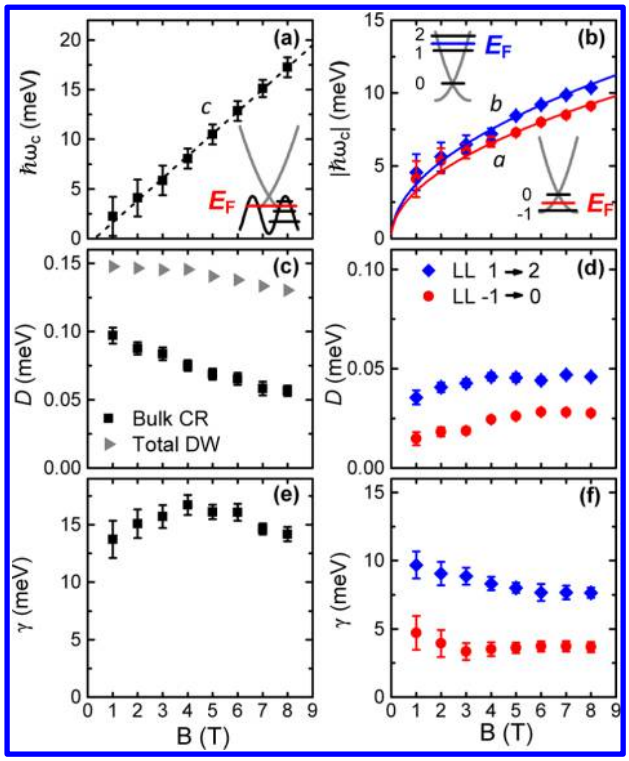

Figure 3. Parameters obtained from the Drude−Lorentz fit of magneto-transmission and Faraday rotation spectra (Figure 1). (a) Transition energies of the CR-like peak for bulk carriers; dashed line is a linear fit to the data. (b) Intraband LL transition energies for SS 1 (red circle) and SS 2 (blue diamond). Solid lines are model curves (eq 1) of $LL_{1\to2}$ and $LL_{-1\to0}$ with $v_F = 2.49 \times 10^5$ and 0.9×10^5 m/s, respectively. Drude weight of the bulk and TSS carriers are displayed in (c) and (d), respectively. The decreasing Drude weight of the bulk CR is unexpected for typical CR transitions. The sum of all three Drude weights is also displayed in (c) as gray triangles. (e,f) Scattering rates for bulk and TSS carriers.

all magnetic fields in Supporting Information Figure S1). We stress that the same model describes the entire data of CR and FR spectra at all different fields. This consistent description of the entire data set attests to the validity of the multicomponent analysis.

The extracted diagonal conductivity σ_{xx} at $B = 0$ and 8 T is plotted in the inset of Figure 2c. As mentioned before, two phonons dominate the low energy conductivity and do not change with the magnetic field. Their frequencies (ω_o), oscillator strengths (ω_p^2), and widths (Γ) are therefore kept constant at their zero field values (listed in Table S1 in Supporting Information) during the fitting at all magnetic fields. The electronic background is modified by the field. Specifically, the spectral weight (SW), defined as $SW = \int_0^{\Omega_c} \sigma_{xx} d\omega$ (Ω_c: cutoff frequency), shifts from low energy (~3 meV) to higher energy (~15 meV) in the $B = 8$ T spectrum. This SW shift is more evident in the field-induced changes of σ_{xx} (Figure 2c). According to the *f*-sum rule,[29] the total SW should be

DOI: 10.1021/acs.nanolett.6b04313
Nano Lett. 2017, 17, 980−984

conserved and independent of magnetic field, given an appropriate Ω_c. Indeed, from Figure 2c we find that the magnetic field induced accumulation of SW around $\hbar\omega_c$ is qualitatively compensated by loss of SW at low energies.

Phonon absorptions also affect the shape of FR spectra at low frequencies, shown in Figure 2b. However, according to eq 3, the Hall conductivity (σ_{xy}) is expected to only contain electronic contributions. Indeed, the σ_{xy} spectra (red line in Figure 2d) extracted via thin-film approximation are free of phonon structures. The extracted total σ_{xy} spectra show an excellent agreement with the three-layer DL model calculation (black dotted line), justifying the use of thin-film approximations (see Supporting Information Sec. I). We now turn to the analysis of the fitting parameters extracted from the three-layer DL description of magneto-optics data. Each layer is parametrized by its own cyclotron frequency ($\hbar\omega_c$), Drude weight (D), and scattering rate (γ). All these contributions are additive in the MO response in the thin-film limit.[10,28]

In Figure 3 we plot the field dependence of $\hbar\omega_c$, D, and γ extracted from simultaneous fitting of the CR and FR spectra at different magnetic fields. This analysis reveals the $\sqrt{B}$-dependence of the transition energy for the two lower energy transitions, shown in Figure 3b. The $\sqrt{B}$ law is the hallmark of LL spacings for massless Dirac fermions, and therefore, we assign these two terms to the response of the TSSs in our films. Notably, this behavior can only be observed provided the Fermi energy is close to the Dirac point when only the lowest few LLs are occupied.[18,30] We thus conclude that the Fermi energies associated with two surfaces in BST are very close to the Dirac point, and we will report estimates of E_F below. In contrast, the broader CR-like transition (Figure 3a) shows conventional linear field dependence. We attribute this latter mode to bulk p-type carriers, as pictured in the inset of Figure 3a. The cyclotron mass extracted from the slope is 0.055 m_e, which is smaller than the effective mass of 0.08 m_e deduced from quantum oscillations for a p-type BST sample.[31] The discrepancy could be due to difference in Fermi energy (BST valence band are nonparabolic[31]) and/or stain in our thin films. Note that there is a peak structure in γ (Figure 3e) around 4 T, where the corresponding $\hbar\omega_c \approx 8$ meV coincides with one of the phonons of BST. It is possible that the peak arises from the scattering between bulk CR and phonon modes, as suggested in a recent terahertz MO study on Bi_2Se_3.[10]

It is worth emphasizing that the transition energies of the two SS transitions (a and b) are fairly close to each other, especially at low fields. We can nevertheless differentiate these two contributions because of the hump structure in the FR spectra, which is characteristic of the two opposite polarization rotations nearly canceling each other. Thus, the FR spectra allow us to unambiguously differentiate and assign these two responses to two different surfaces.

The evolution of Drude weight and scattering rate of the two SS transitions with field are intriguing as well (Figures 3d,f). Both Drude weights increase with increasing magnetic field, in accord with the theoretical prediction for Dirac fermions.[21] In contrast, the Drude weight for semiclasical CR is usually field-independent and equals the zero-field Drude weight.[30] The scattering rates of the two SS transitions decrease with B field and show an overall $1/B$ dependence, which is indicative of charged impurity scattering.[32,33] The scattering rates of the TSS carriers are also much smaller than their bulk counterpart, indicating much higher mobility associated with the surface states.

The requirement of E_F lying very close to the Dirac point ($\sqrt{B}$ dispersion) constrains the assignment of the observed SS Landau level transitions to two possibilities: $LL_{0\to1}$ and $LL_{1\to2}$ or alternatively $LL_{-1\to0}$ and $LL_{-2\to-1}$ for hole-like transitions. Higher intraband LL transitions ($|n| \geqslant 2$) are excluded for two reasons: (i) At $|n| \approx 2$, these transitions are expected to produce discontinuous jumps in transition energy that are not observed in our data; (ii) At $|n| \gg 2$, corresponding to high Fermi energy, the evolution of the transition energy with the B field resembles the linear scaling (quasi-classical CR),[34] whereas our data show the $\sqrt{B}$ behavior, requiring low Fermi energy. Fitting the two SS transitions with linear dependence will result in finite intercept in energy, contrary to the semiclassical CR picture. However, fits with $\sqrt{B}$ dependence show excellent agreement with experimental transitions energies (Figure 3b). Since the n-type SS transition also has higher Drude weight than the p-type SS, we attribute the former to $LL_{1\to2}$ and the latter to $LL_{-1\to0}$, with $E_F \approx 25$ and -6 meV away from the Dirac point, respectively (see Supporting Information Figures S3 and S4).

The $\sqrt{B}$ fitting in Figure 3b assumes a Fermi velocity of 2.49×10^5 m/s (0.9×10^5 m/s) for the n-type (p-type) TSS. The v_F of our n-type TSS is very close to the ARPES value of 2.2×10^5 m/s on an n-type Sb_2Te_3/Bi_2Te_3 bilayer film with similar E_F (~30 meV).[35] Due to the electron−hole asymmetry, v_F is expected to be smaller on the hole side of the Dirac cone, consistent with our smaller estimated v_F for the p-type TSS.

Finally, we wish to remark on possible relevance of our findings to the hypothesis of chiral magnetic effect.[36,37] It was conjectured that TSSs separating bulk from vacuum become oppositely charged in applied magnetic field, qualitatively consistent with our data. The carrier density on the two surfaces was predicted to scale linearly with the magnetic field, also in approximate agreement with our data (Figure 3d) at $B <$ 5 T. The induced densities flatten off at $B >$ 5 T, likely due to the screening of finite bulk charge carriers. This hypothesis has implications for the finite frequency response of a TI: a resonance mode can be anticipated in infrared frequencies, offering yet another opportunity to investigate the condensed matter manifestations of phenomena discussed in high energy physics. The search for such resonances remains a challenge for future theoretical and experimental studies of 3D-TIs as well as Dirac/Weyl semimetals[38,39] in magnetic field.

In conclusion, we optically distinguished coexisting TSSs and bulk carriers in BST from their different LL transition dynamics in magnetic field. Our results also show that the Fermi levels for the TSSs are remarkably low, allowing for the observation of $\sqrt{B}$ behavior characteristic of intraband LL transition. Importantly, the top and bottom TSS host carriers of opposite type, separated by the bulk. Such separated n- and p-type Dirac fermions pave the way for the observation of exotic quantum phenomena in TI, such as topological magneto-electric effect[40] and topological exciton condensation.[22]

■ ASSOCIATED CONTENT

Supporting Information

The Supporting Information is available free of charge on the ACS Publications website at DOI: 10.1021/acs.nanolett.6b04313.

Sample and experimental details. Fitted magneto-transmission and Faraday rotation at all measured magnetic

DOI: 10.1021/acs.nanolett.6b04313
Nano Lett. 2017, 17, 980−984

fields. Models of Landau level transitions. Discussion about thin film approximation and Zeeman effect (PDF)

AUTHOR INFORMATION

Corresponding Author

*E-mail: shaoyinming@gmail.com. Phone: +1(858)9008637.

ORCID

Yinming Shao: 0000-0002-2891-0028

Notes

The authors declare no competing financial interest.

ACKNOWLEDGMENTS

This work is supported by DOE Grant No. DE-FG02-00ER45799. Sample growth and characterization at Penn State was supported by ONR (Grant No. N00014-15-1-2370) and ARO-MURI (Grant No. W911NF-12-1-0461). D.K. is supported by DOE Grants No. DE-FG-88ER40388 and DE-SC0012704. D.N.B. is the Moore Foundation Investigator, EPIQS Initiative Grant GBMF4533.

REFERENCES

(1) Hasan, M. Z.; Kane, C. L. *Rev. Mod. Phys.* **2010**, *82*, 3045−3067.
(2) Qi, X.-L.; Zhang, S.-C. *Rev. Mod. Phys.* **2011**, *83*, 1057−1110.
(3) Moore, J. E. *Nature* **2010**, *464*, 194−198.
(4) Hsieh, D.; et al. *Nature* **2009**, *460*, 1101−1105.
(5) Kong, D.; Chen, Y.; Cha, J. J.; Zhang, Q.; Analytis, J. G.; Lai, K.; Liu, Z.; Hong, S. S.; Koski, K. J.; Mo, S.-K.; Hussain, Z.; Fisher, I. R.; Shen, Z.-X.; Cui, Y. *Nat. Nanotechnol.* **2011**, *6*, 705−709.
(6) Zhang, J.; Chang, C.-Z.; Zhang, Z.; Wen, J.; Feng, X.; Li, K.; Liu, M.; He, K.; Wang, L.; Chen, X.; Xue, Q.-K.; Ma, X.; Wang, Y. *Nat. Commun.* **2011**, *2*, 574.
(7) Cheng, P.; et al. *Phys. Rev. Lett.* **2010**, *105*, 076801.
(8) Jiang, Y.; Wang, Y.; Chen, M.; Li, Z.; Song, C.; He, K.; Wang, L.; Chen, X.; Ma, X.; Xue, Q.-K. *Phys. Rev. Lett.* **2012**, *108*, 016401.
(9) Post, W. K.; Chapler, C. B.; Liu, K. M.; Wu, S. J.; Stinson, T. H.; Goldflam, D. M.; Richardella, R. A.; Lee, S. J.; Reijnders, A. A.; Burch, S. K.; Fogler, M. M.; Samarth, N.; Basov, N. D. *Phys. Rev. Lett.* **2015**, *115*, 116804.
(10) Wu, L.; Tse, W.-K.; Brahlek, M.; Morris, M. C.; Aguilar, R. V.; Koirala, N.; Oh, S.; Armitage, P. N. *Phys. Rev. Lett.* **2015**, *115*, 217602.
(11) Di Pietro, P.; Vitucci, F. M.; Nicoletti, D.; Baldassarre, L.; Calvani, P.; Cava, R.; Hor, Y. S.; Schade, U.; Lupi, S. *Phys. Rev. B: Condens. Matter Mater. Phys.* **2012**, *86*, 045439.
(12) He, X.; Guan, T.; Wang, X.; Feng, B.; Cheng, P.; Chen, L.; Li, Y.; Wu, K. *Appl. Phys. Lett.* **2012**, *101*, 123111.
(13) Lin, C. J.; He, X. Y.; Liao, J.; Wang, X. X.; Sacksteder, V., IV; Yang, W. M.; Guan, T.; Zhang, Q. M.; Gu, L.; Zhang, G. Y.; Zeng, C. G.; Dai, X.; Wu, K. H.; Li, Y. Q. *Phys. Rev. B: Condens. Matter Mater. Phys.* **2013**, *88*, 041307.
(14) He, L.; Kou, X.; Lang, M.; Choi, E. S.; Jiang, Y.; Nie, T.; Jiang, W.; Fan, Y.; Wang, Y.; Xiu, F.; Wang, K. L. *Sci. Rep.* **2013**, *3*, 3406.
(15) Basov, D. N.; Timusk, T. *Rev. Mod. Phys.* **2005**, *77*, 721−779.
(16) Levallois, J.; Nedoliuk, I. O.; Crassee, I.; Kuzmenko, A. B. *Rev. Sci. Instrum.* **2015**, *86*, 033906.
(17) Crassee, I.; Levallois, J.; van der Marel, D.; Walter, A. L.; Seyller, T.; Kuzmenko, A. B. *Phys. Rev. B: Condens. Matter Mater. Phys.* **2011**, *84*, 035103.
(18) Crassee, I.; Levallois, J.; Walter, A. L.; Ostler, M.; Bostwick, A.; Rotenberg, E.; Seyller, T.; van der Marel, D.; Kuzmenko, A. B. *Nat. Phys.* **2011**, *7*, 48−51.
(19) Jiang, Z.; Henriksen, E. A.; Tung, L. C.; Wang, Y.-J.; Schwartz, M. E.; Han, M. Y.; Kim, P.; Stormer, H. L. *Phys. Rev. Lett.* **2007**, *98*, 197403.
(20) Li, Z.; Carbotte, J. P. *Phys. Rev. B: Condens. Matter Mater. Phys.* **2013**, *88*, 045414.
(21) Gusynin, V. P.; Sharapov, S. G.; Carbotte, J. P. *J. Phys.: Condens. Matter* **2007**, *19*, 026222.
(22) Seradjeh, B.; Moore, J. E.; Franz, M. *Phys. Rev. Lett.* **2009**, *103*, 066402.
(23) Tse, W.-K.; MacDonald, A. H. *Phys. Rev. B: Condens. Matter Mater. Phys.* **2011**, *84*, 205327.
(24) Morimoto, T.; Hatsugai, Y.; Aoki, H. *Phys. Rev. Lett.* **2009**, *103*, 116803.
(25) Shuvaev, A.; Dziom, V.; Kvon, D. Z.; Mikhailov, N. N.; Pimenov, A. *Phys. Rev. Lett.* **2016**, *117*, 117401.
(26) Okada, K. N.; Takahashi, Y.; Mogi, M.; Yoshimi, R.; Tsukazaki, A.; Takahashi, K. S.; Ogawa, N.; Kawasaki, M.; Tokura, Y. *Nat. Commun.* **2016**, *7*, 12245.
(27) Wu, L.; Salehi, M.; Koirala, N.; Moon, J.; Oh, S.; Armitage, N. P. *Science* **2016**, *354*, 1124−1127.
(28) Shimano, R.; Yumoto, G.; Yoo, J. Y.; Matsunaga, R.; Tanabe, S.; Hibino, H.; Morimoto, T.; Aoki, H. *Nat. Commun.* **2013**, *4*, 1841.
(29) Basov, D. N.; Averitt, R. D.; van der Marel, D.; Dressel, M.; Haule, K. *Rev. Mod. Phys.* **2011**, *83*, 471−541.
(30) Orlita, M.; Crassee, I.; Faugeras, C.; Kuzmenko, A. B.; Fromm, F.; Ostler, M.; Seyller, T.; Martinez, G.; Polini, M.; Potemski, M. *New J. Phys.* **2012**, *14*, 095008.
(31) Köhler, H.; Freudenberger, A. *Phys. Status Solidi B* **1977**, *84*, 195−203.
(32) Yang, C. H.; Peeters, F. M.; Xu, W. *Phys. Rev. B: Condens. Matter Mater. Phys.* **2010**, *82*, 075401.
(33) Orlita, M.; Faugeras, C.; Grill, R.; Wysmolek, A.; Strupinski, W.; Berger, C.; de Heer, W. A.; Martinez, G.; Potemski, M. *Phys. Rev. Lett.* **2011**, *107*, 216603.
(34) Witowski, A. M.; Orlita, M.; Stępniewski, R.; Wysmołek, A.; Baranowski, J. M.; Strupiński, W.; Faugeras, C.; Martinez, G.; Potemski, M. *Phys. Rev. B: Condens. Matter Mater. Phys.* **2010**, *82*, 165305.
(35) Eschbach, M.; et al. *Nat. Commun.* **2015**, *6*, 8816.
(36) Kharzeev, D. E. *Ann. Phys.* **2010**, *325*, 205−218.
(37) Qi, X.-L.; Hughes, T. L.; Zhang, S.-C. *Phys. Rev. B: Condens. Matter Mater. Phys.* **2008**, *78*, 195424.
(38) Kargarian, M.; Randeria, M.; Trivedi, N. *Sci. Rep.* **2015**, *5*, 12683.
(39) Akrap, A.; et al. *Phys. Rev. Lett.* **2016**, *117*, 136401.
(40) Morimoto, T.; Furusaki, A.; Nagaosa, N. *Phys. Rev. B: Condens. Matter Mater. Phys.* **2015**, *92*, 085113.

DOI: 10.1021/acs.nanolett.6b04313
Nano Lett. 2017, 17, 980−984

Supporting Information for: Faraday rotation due to surface states in the topological insulator $(Bi_{1-x}Sb_x)_2Te_3$

Yinming Shao,[*,†] Kirk W. Post,[‡] Jhih-Sheng Wu,[‡] Siyuan Dai,[‡] Alex J. Frenzel,[‡] Anthony R. Richardella,[¶] Joon Sue Lee,[¶] Nitin Samarth,[¶] Michael M. Fogler,[‡] Alexander V. Balatsky,[§,‖] Dmitri E. Kharzeev,[⊥,#] and D. N. Basov[†,‡]

†*Department of Physics, Columbia University, New York, New York 10027, United States*

‡*Physics Department, University of California-San Diego, La Jolla, California 92093, United States*

¶*Department of Physics, The Pennsylvania State University, University Park, Pennsylvania 16802, United States*

§*Nordita, KTH Royal Institute of Technology and Stockholm University, Roslagstullsbacken 23, SE-106 91 Stockholm, Sweden*

‖*Institute for Materials Science, Los Alamos National Laboratory, Los Alamos, New Mexico 87545, United States*

⊥*Department of Physics and Astronomy, Stony Brook University, Stony Brook, New York 11794-3800, United States*

#*Department of Physics and RIKEN-BNL Research Center, Brookhaven National Laboratory, Upton, New York 11973, United States*

*Corresponding author: Yinming Shao (shaoyinming@gmail.com)

Phone: +1(858)9008637

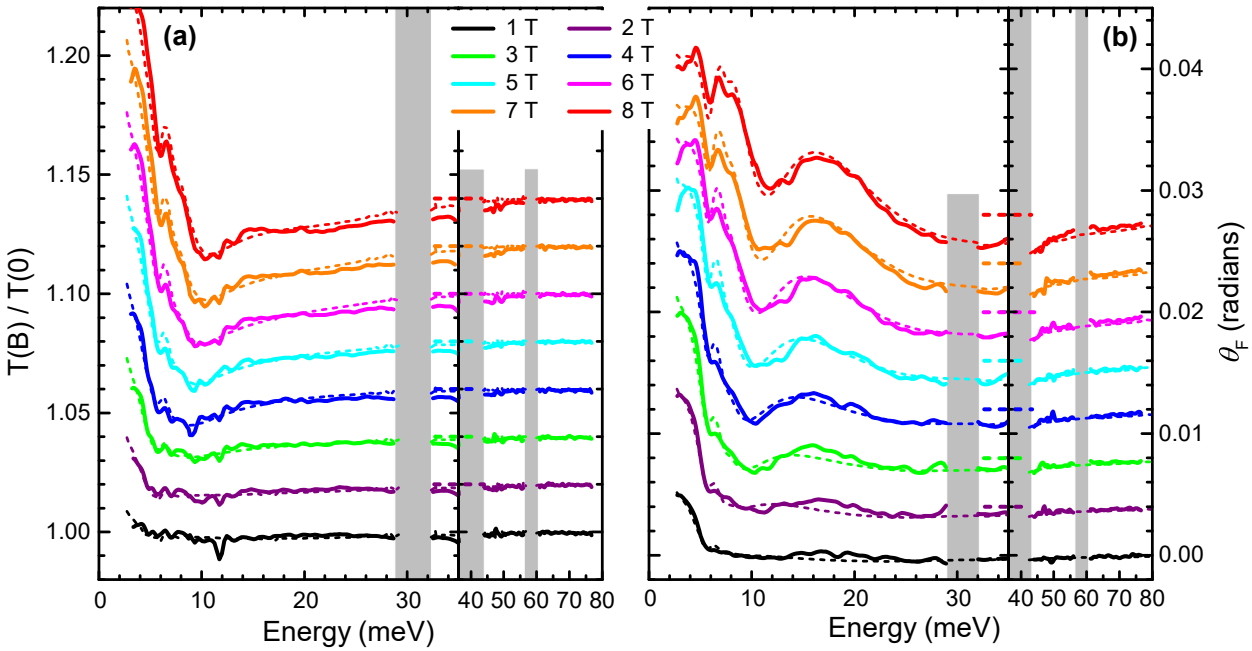

Figure S1: Modeled (short dashed line) magneto-transmission (a) and Faraday rotation (b) curves overlaid on raw data (solid line) for all measured magnetic fields (1 - 8 T).

I. Experimental details and Thin-film approximation

The $(Bi_{1-x}Sb_x)_2Te_3$ (BST, x=0.54) films (58 nm) are grown on InP (111)A substrates. A ∼10 nm amorphous Se capping layer was deposited on top of the BST film to protect it from exposure to atmosphere.[1,2] The capping layer is not removed to keep the film in its pristine form for all magneto-optical measurements. Far-infrared transmission spectra of large area (∼4 mm^2) BST samples were measured in zero and finite magnetic fields (0 T to 8 T) using a Fourier transform spectrometer coupled to an 8 T split-coil superconducting magnet. Transmitted radiation was detected by a He-cooled bolometer maintained at 1.6 K and 4.2 K for THz and far-IR frequencies, respectively. Faraday geometry (light propagating along c axis and B//c axis) was used for all the transmission measurements. The sample and substrate temperature were maintained at T = 15K using a Helium flow cryostat.

Faraday rotation spectra were measured in the same frequency range and temperature as the transmission spectra using a crossed polarizer technique[3] where a polarizer is placed both before and after the sample. These polarizers could be rotated to measure the angu-

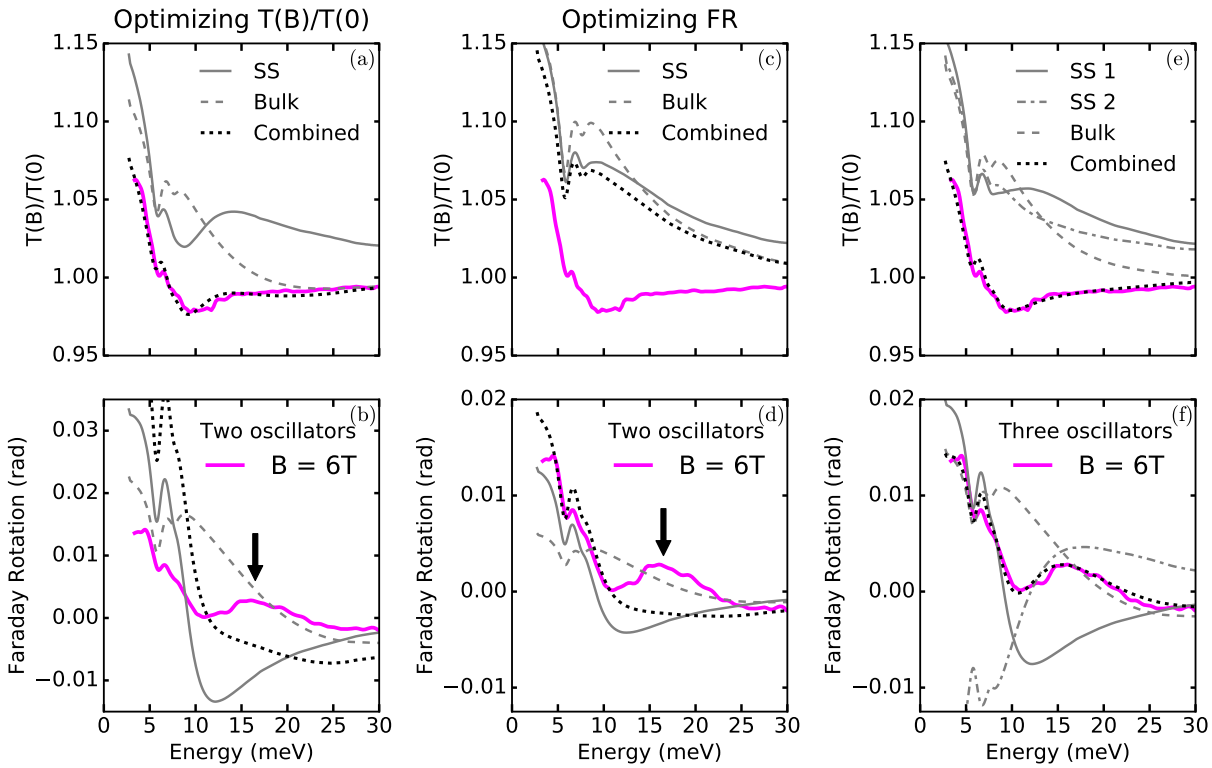

Figure S2: Solid magenta lines in all panels are experimental data: (top panels) zero-field normalized transmission T(B)/T(0) (CR) at 6T; (bottom panels) Faraday rotation (FR) at 6T. The two oscillator model can only reproduce some features in CR and FR spectra; therefore fits in panels (a) and (b) are optimized for CR spectra, while fits in panels (c) and (d) are optimized for FR spectra. Black arrows in (b) and (d) indicate the hump feature in FR that is not reproduced by two oscillator models. Panels (e) and (f) are fits with three oscillator model, showing excellent agreement between model and data.

lar dependence of the transmitted radiation. Both polarities of the magnet were used to eliminate spurious rotation signal arising from the optical elements.

The real parts of the diagonal (Hall conductivity) can be directly extracted from experimentally measured substrate-normalized transmission (Faraday rotation) spectra, using the thin-film approximation:[4–6]

$$T(\omega, B) \approx \left[1 + \frac{2}{1+n_s}\frac{1+t^4r^3}{1-t^4r^4}\mathrm{Re}(Z_0 G_{xx})\right]^{-1} \tag{1}$$

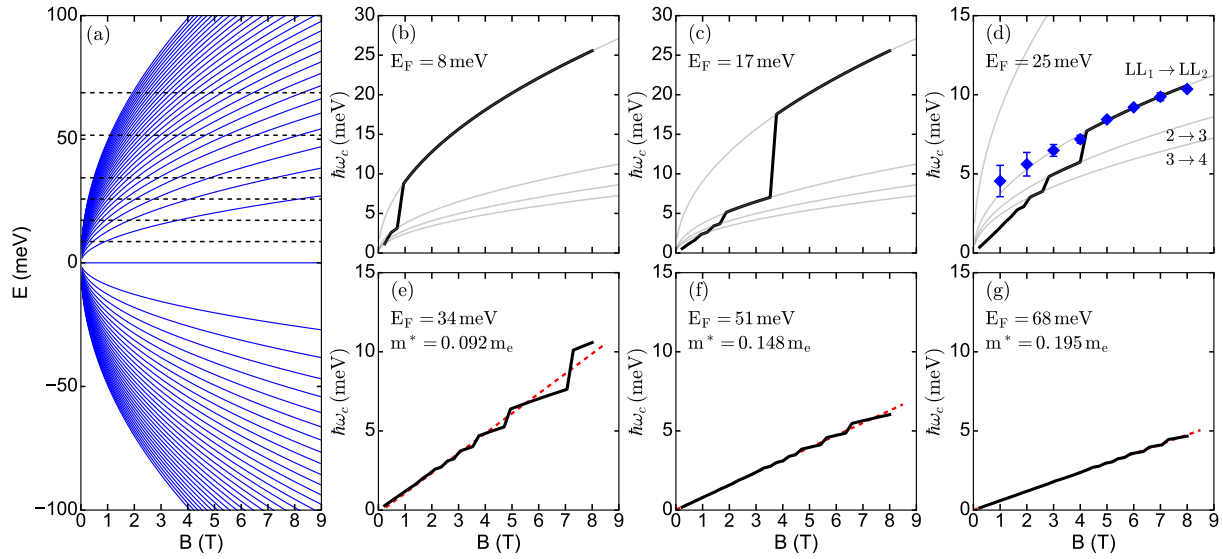

Figure S3: Calculated Landau-level fan diagram (a) from a pure Dirac band with v_F=2.49 × 10^5 m/s. Black dashed lines in (a) are line cuts at different Fermi energy, around each Fermi energy the intraband LL transition allowed by selection rule are plotted in panel (b)-(d) and panel (e)-(g) as black solid lines. In low Fermi energy region (b)-(d), the intraband LL transition energy follow $\sqrt{B}$ relation with magnetic field, with jumps when Fermi energy crosses a LL. In high Fermi energy region (e)-(g) the transition energy scales linearly with magnetic field and enters the quasi-classical region. Red line in (e)-(g) are linear fit using $\omega_c = eB/m^*$. In panel (d) the experimental data for the n-type intraband LL transition was overlaid on top of the model.

Table S1: BST phonon parameters extracted from zero field transmission spectra

	Phonon energy ω_o (meV)	Oscillator strength ω_p^2 ($10^5\,cm^{-2}$)	width Γ (meV)
1	5.90	5.129	0.94
2	7.66	1.624	1.22

$$\theta_F(\omega, B) \approx \frac{\mathrm{Re}(Z_0 G_{xy})}{1 + n_s + \mathrm{Re}(Z_0 G_{xx})} \tag{2}$$

where $t(\omega)$=exp$(-\omega k_s d_s/c)$, $r(\omega) = (n_s - 1)/(n_s + 1)$, $G_{xx/xy} = \sigma_{xx/xy} \cdot d$ is the diagonal/Hall conductance, Z_0 is the impedance of vacuum and d is the thickness of the film. In Eq. (4), $n_s(\omega)$, $k_s(\omega)$ and d_s are the refractive index, extinction coefficient, and thickness of the substrate. Note that unlike graphene, phonons dominate the low energy diagonal conductivity in BST, so that G_{xx} cannot be ignored in the expression of θ_F. The wavelength of far-IR light ($\sim$10$-$500 μm) is much larger than the sample thickness ($\sim$1 nm/58 nm for SS/bulk),

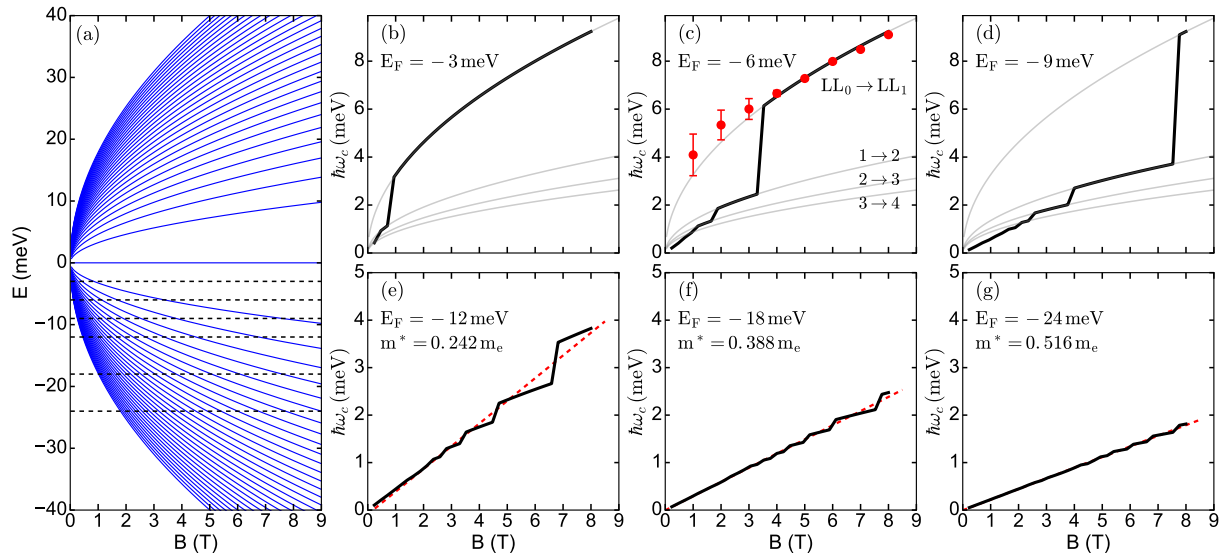

Figure S4: Calculated Landau-level fan diagram (a) from a pure Dirac band with v_F=0.9×10^5 m/s. Black dashed lines in (a) are line cuts at different Fermi energy, around each Fermi energy the intraband LL transition allowed by selection rule are plotted in panels (b)-(d) and panels (e)-(g) as black solid lines. In low Fermi energy region (b)-(d), the intraband LL transition energy follow $\sqrt{B}$ relation with magnetic field, with jumps when Fermi energy crosses an LL. In high Fermi energy region (e)-(g) the transition energy scales linearly with magnetic field and enters the quasi-classical region. Red line in (e)-(g) are linear fit using $\omega_c = eB/m^*$. In panel (c) the experimental data for the p-type intraband LL transition was overlaid on top of the model.

so responses from different layers effectively add up in the MO response.

II. Comparison of two oscillator and three oscillator model

The fitted CR and FR spectra (dashed lines) are overlaid on top of raw spectra (solid lines) for all measured magnetic fields, as shown in Figure S1. The phonon parameters (listed in Table S1) are deduced from zero-field transmission measurements, in agreement with previous values.[1,7] Phonon parameters are fixed to be zero-field values for fitting CR and FR spectra.

To further illustrate the necessity of three oscillators to fit both CR and FR spectra, we compare the fitting results of two and three oscillator model with experimental spectra. In

Figure S2, the solid magenta lines in all panels are CR (top panels) and FR (bottom panels) spectra at B = 6 T.

Panels (a) - (d) show two oscillator model fits with different fitting parameters. Since the two oscillator model can only capture some features in CR and FR spectra, the fits are optimized for either T(B)/T(0) or FR, shown in panels (a), (b) and (c), (d), respectively.

For example, in panel (a) where the CR spectrum is well reproduced by the two oscillator model, the corresponding FR model (black dotted line in (b)) is in stark contrast with experiment. The modeled low frequency FR is about three times the experimental value and the hump feature in FR data (black arrow in (b)) is not reproduced. One can reduce the spectra weight of both oscillators to match the FR data in amplitude, as illustrated by the black dotted line in (d). However, the hump feature is still not reflected in the model. Moreover, this artificially reduced spectral weights also lead to significantly reduced absorption (enhanced transmission) compared to zero field transmission, as reflected in panel (c).

The rightmost column depicts the fitting result with three oscillator model for B=6T, showing excellent agreement between model and both CR (e) and FR (f) spectra. As mentioned in the main text, the hump feature constitutes direct evidence of a third electron-like carrier channel, which has FR angle opposite to hole-like carriers.

III. Additive Faraday rotation under the limit $\theta_F \ll 1$ radian

In this section we present a simple derivation of the additive nature of small Faraday rotation angle assumed in the main text. Let the incoming light be polarized in x direction, within

the Jones matrix formalism, the light after two rotation can be expressed as:

$$\begin{bmatrix} E_x \\ E_y \end{bmatrix} = \begin{bmatrix} t_{2x} & -t_{2y} \\ t_{2y} & t_{2x} \end{bmatrix} \begin{bmatrix} t_{1x} & -t_{1y} \\ t_{1y} & t_{1x} \end{bmatrix} \begin{bmatrix} E_0 \\ 0 \end{bmatrix} = \begin{bmatrix} E_0(t_{1x}t_{2x} - t_{1y}t_{2y}) \\ E_0(t_{1x}t_{2y} + t_{1y}t_{2x}) \end{bmatrix}$$

where t_x and t_y are the transmission coefficient of x- and y-polarized component. Assuming $\theta_F \ll 1$ rad, we have $t_{yx} \ll t_{xx}$ and $\theta_F = \arctan(t_{yx}/t_{xx}) \approx t_{yx}/t_{xx}$. Therefore the total rotation $\theta_{F,total}$:

$$\arctan(\frac{t_{1x}t_{2y} + t_{1y}t_{2x}}{t_{1x}t_{2x} - t_{1y}t_{2y}}) \approx \arctan(\frac{t_{2y}}{t_{2x}} + \frac{t_{1y}}{t_{1x}}) = \frac{t_{2y}}{t_{2x}} + \frac{t_{1y}}{t_{1x}} = \theta_{F1} + \theta_{F2}$$

IV. Zeeman effect and electron-hole asymmetry

In general, the ideal Dirac LL spectrum (main text Eq. (1)) can be modified by considering Zeeman effect and electron-hole asymmetry bands. The Hamiltonian for this non-ideal Dirac fermion can be written as:[8]

$$\hat{H} = \frac{\Pi^2}{2m^*} + v_F(\sigma_x\Pi_y - \sigma_y\Pi_x) + \frac{1}{2}g_s\mu_B B\sigma_z \tag{3}$$

The corresponding LL spectrum is then expressed as:

$$\begin{aligned} E_{\pm n\neq 0} &= n\hbar\omega_c \pm \sqrt{2e\hbar v_F^2|n|B + (\frac{1}{2}\hbar\omega_c - \frac{1}{2}g_s\mu_B B)^2} \\ E_{n=0} &= \frac{1}{2}\hbar\omega_c - \frac{1}{2}g_s\mu_B B \end{aligned} \tag{4}$$

where the cyclotron frequency $\omega_c = eB/m^*$ comes from the parabolic term in $\hat{H}$ and $\Delta = g_s\mu_B B/2$ is the Zeeman energy for surface g-factor g_s. Note that unlike graphene and conventional two-dimensional electron gas, the LLs of TSS are spin-polarized and therefore will shift instead of split when Zeeman effect is included.[9,10]

When finite curvature is considered, depending on the relative value of g_s and quadratic

effective mass m^*, the LLs can be moved up, down, or even unchanged compared to the ideal case $E_{\pm n} = \pm\sqrt{2e\hbar v_F^2|n|B}$. However, the experimental value of g_s for TSS has been controversial and inconsistent, ranging from 2 to 76 for the same materials.[8,11] Using $g_s = 11$ for Sb_2Te_3[9] and assuming the electron-hole asymmetry is negligible, the 0th LL will shift downward $\Delta = g_s\mu_B B/2$ ~2.5 meV at 8 T. Such shift would result in slightly larger v_F in order to match the same transition energy. For the p-type $LL_{-1\to0}$ transition, the fitted Fermi velocity is increased to $v_F = 1.1 \times 10^5$ m/s when considering the Zeeman effect. Similar shift is drastically decreased for higher LLs, since $\delta E_{\pm n} \approx \pm\Delta^2/2\sqrt{2e\hbar v_F^2|n|B}$ for $\Delta < \sqrt{2e\hbar v_F^2|n|B}$.[10]

References

(1) Post, W., K. Chapler, C., B. Liu, K., M. Wu, S., J. Stinson, T., H. Goldflam, D., M. Richardella, R., A. Lee, S., J. Reijnders, A., A. Burch, S., K. Fogler, M., M. Samarth, N.; Basov, N., D. *Phys. Rev. Lett.* **2015**, *115*, 116804.

(2) Wu, L.; Brahlek, M.; Valdés Aguilar, R.; Stier, A. V.; Morris, C. M.; Lubashevsky, Y.; Bilbro, L. S.; Bansal, N.; Oh, S.; Armitage, N. P. *Nat Phys* **2013**, *9*, 410–414.

(3) Levallois, J.; Nedoliuk, I. O.; Crassee, I.; Kuzmenko, A. B. *Rev. Sci. Instrum.* **2015**, *86*, 033906.

(4) Crassee, I.; Levallois, J.; van der Marel, D.; Walter, A. L.; Seyller, T.; Kuzmenko, A. B. *Phys. Rev. B* **2011**, *84*, 035103.

(5) O'Connell, R. F.; Wallace, G. *Phys. Rev. B* **1982**, *26*, 2231–2234.

(6) Jenkins, G. S.; Schmadel, D. C.; Drew, H. D. *Rev. Sci. Instrum.* **2010**, *81*, 083903.

(7) Richter, W.; Becker, C. R. *phys. stat. sol. (b)* **1977**, *84*, 619–628.

(8) Taskin, A. A.; Ando, Y. *Phys. Rev. B* **2011**, *84*, 035301.

(9) Yoshimi, R.; Tsukazaki, A.; Kikutake, K.; Checkelsky, J. G.; Takahashi, K. S.; Kawasaki, M.; Tokura, Y. *Nat. Mater.* **2014**, *13*, 253–257.

(10) Fu, Y.-S.; Hanaguri, T.; Igarashi, K.; Kawamura, M.; Bahramy, M. S.; Sasagawa, T. *Nat. Commun.* **2016**, *7*, 10829.

(11) Xiong, J.; Luo, Y.; Khoo, Y.; Jia, S.; Cava, R. J.; Ong, N. P. *Phys. Rev. B* **2012**, *86*, 045314.